DOI 10.1007/s11182-020-01874-2

Russian Physics Journal, Vol. 62, No. 9, January, 2020 (Russian Original No. 9, September, 2019)

CONDENSED-STATE PHYSICS

PLASTIC STRAIN LOCALIZATION IN POLYCRYSTALLINE TITANIUM. NUMERICAL SIMULATION

E. S. Emelianova,[1,2] V. A. Romanova,[1] R. R. Balokhonov,[1] and M. V. Sergeev[2] UDC 539.3

The paper presents numerical simulation of polycrystalline titanium deformation in terms of the crystal plasticity theory. Based on the experimental data, a three-dimensional polycrystalline model is generated by a method of step-by-step packing. Constitutive relations for the deformation behavior of grains are based on the crystal plasticity theory with regard to the crystalline structure and dislocation glide in hexagonal close-packed crystal lattices. The boundary value problem of elastoplastic deformation is solved numerically using the finite element method. The proposed model is tested by elastoplastic deformation of titanium single crystals having different orientation. The proposed model is used to study the influence of the crystallographic orientation on localized plastic deformation in polycrystals.

Keywords: micromechanics, crystal plasticity, polycrystalline structure, numerical simulation, localized deformation.

INTRODUCTION

In the framework of contemporary understanding of the load-induced deformation and fracture processes in materials, their microstructure plays a critical role. Experimental and theoretical data indicate that the material interfaces cause microstress concentrations that can differ by an order of magnitude from an average value. It is a microstress concentration that causes irreversible deformation and microcrack initiation. Irreversible deformation at lower scale levels generates the material response at higher scale levels. Thus, early-predicted irreversible macroscale deformation and fracture require knowledge of the deformation response at the micro- and mesoscales.

Along with experimental, numerical simulation is an important tool for studying deformation processes in materials developing at different scales. With regard to numerical simulation, a key challenge is the development of constitutive models allowing to describe the deformation behavior of materials.

It is important for the models to describe the plastic behavior of polycrystalline materials having significant anisotropy of elastoplastic properties attributed to the crystalline structure, materials having the restricted number of slip systems, and textured metals and alloys. Such models are developed in terms of the crystal plasticity which considers the relation between the stress-strain state and physical (dislocation) mechanisms of plastic flow at the microscale.

The existing models of crystal plasticity can be divided into two groups. The first group aims to construct constitutive relations for the description of averaged response of the material with regard to the contribution from grains oriented in various directions [1, 2]. More complicated models of this type are being currently developed; they consider contributions from deformation mechanisms at different scales, the mesoscale, in particular [3]. These models are

[1]Institute of Strength Physics and Materials Science of the Siberian Branch of the Russian Academy of Sciences, Tomsk, Russia, e-mail: emelianova@ispms.tsc.ru; Varvara@ispms.tsc.ru; rusy@ispms.tsc.ru; [2]National Research Tomsk State University, Tomsk, Russia, e-mail: sergeevmaximv@gmail.com. Translated from Izvestiya Vysshikh Uchebnykh Zavedenii, Fizika, No. 9, pp. 3–14, September, 2019. Original article submitted June 25, 2019.

important for analyzing the deformation-induced texture evolution, response of textured materials during pressure forming or other kinds of plastic deformation. These approaches, however, cannot evaluate local stress and strain values. Such problems can be solved by using another type of the crystal plasticity models that involve boundary value problems explicitly subject to the microstructure [4–6]. Such models allow users to explicitly study the evolution of local characteristics of the stress-strain state under load.

This paper proposes the crystal plasticity approach with explicit subject consideration of the material microstructure to ascertain the properties of the deformation behavior of polycrystalline titanium. As is known, titanium and titanium alloys with a hexagonal close-packed (HCP) crystal lattice have highly anisotropic elastoplastic properties [7–10]. It is therefore very important to use methods which consider plastic flow contributions at the microscale. The purpose of this work is to explain the influence of the crystallographic texture on the plastic strain localization under the uniaxial load of polycrystalline titanium.

1. MATHEMATICAL PROBLEM FORMULATION AND NUMERICAL SIMULATION

1.1. Three-dimensional boundary value problem

The solution of micromechanical problems explicitly subject to the material microstructure requires high computation capacity. One of the approaches allowing to significantly minimize the requirements for random-access memory, disc space and processing speed is the simulation of quasi-static deformation in terms of dynamics. The solution of such problems provides a transfer from implicit to explicit time integration schemes, thereby giving advantages to solution of nonlinear problems. The applicability of dynamic approaches to modelling quasi-static deformation in materials with inner boundaries is thoroughly investigated in [11]. Using a polycrystalline aluminum alloy, it is shown that the solutions of the dynamic and statistic problems are closely identical providing smooth growth in dynamic load and elimination of the material sensitivity to the strain rate. In our work, we use the dynamic problem to simulate the quasi-static deformation of commercially pure titanium.

The boundary value problem includes equations of motion:

$$\rho \dot{U}_i = \sigma_{ij,j}\,, \tag{1}$$

the equation of continuity:

$$\frac{\dot{V}}{V} - U_{i,i} = 0\,, \tag{2}$$

the kinematic relations for total strain rates:

$$\dot{\varepsilon}_{ij} = \frac{1}{2}\left(U_{i,j} + U_{j,i}\right) \tag{3}$$

and constitutive relations in the rate form of generalized Hooke's law for an anisotropic elastoplastic material:

$$\dot{\sigma}_{ij} = C_{ijkl}\left(\dot{\varepsilon}_{kl} - \dot{\varepsilon}^{p}_{kl}\right). \tag{4}$$

Here U_i is the velocity vector, V is the relative volume, ρ is the current density of the material, σ_{ij} is the stress tensor, ε_{ij} and ε^{p}_{ij} are the total and plastic strain tensors, respectively, C_{ijkl} is the tensor of elastic moduli.

The system of equations (1)–(4) is closed by the boundary conditions given on S_U and S_T surfaces in rates:

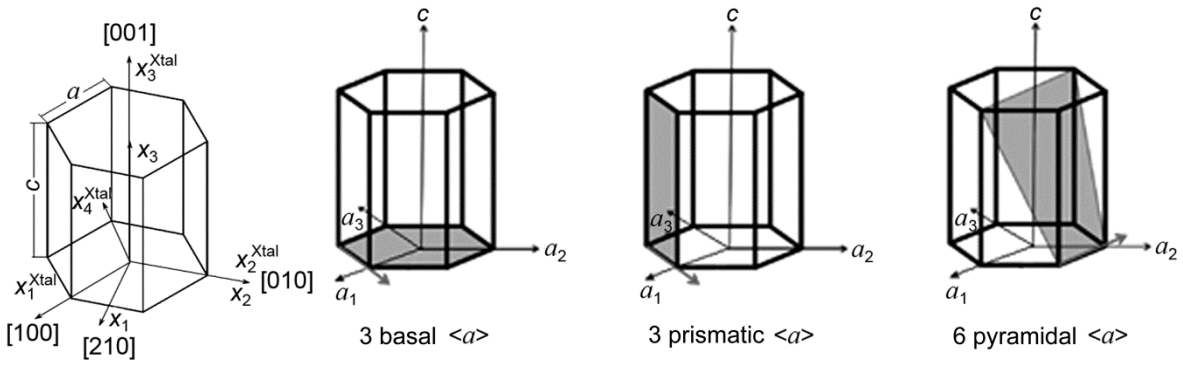

Fig. 1. Schematic of HCP crystal (*a*) and different slip systems (*b*).

$$U_i\big|_{S_U} = u^* \tag{5}$$

and forces:

$$\sigma_{ij} n_j\big|_{S_T} = T_i . \tag{6}$$

The loading conditions applied in calculations are discussed in Section 2.

1.2. Crystal plasticity-based constitutive relations for HCP crystals

Titanium has an HCP crystal lattice schematically shown in Fig. 1*a*. Let us write constitutive relations (Eq. (4)) for titanium single crystal relative to the orthogonal coordinate system x_i, where the axes coincide with $[210]$, $[010]$ and $[001]$ crystallographic directions. The matrix of elastic moduli of HCP crystals has twelve non-zero constants; five of them are independent, namely: C_{1111}, C_{1122}, C_{1133}, C_{3333} and C_{2323}. Titanium single crystals are cannot be deformed by the dislocation glide along x_3^{Xtal} axis (Fig. 1*a*). In this regard, the constitutive relations take the form

$$\begin{aligned}
\dot{\sigma}_{11} &= C_{1111}(\dot{\varepsilon}_{11} - \dot{\varepsilon}_{11}^p) + C_{1122}(\dot{\varepsilon}_{22} - \dot{\varepsilon}_{22}^p) + C_{1133}\dot{\varepsilon}_{33}, \\
\dot{\sigma}_{22} &= C_{1122}(\dot{\varepsilon}_{11} - \dot{\varepsilon}_{11}^p) + C_{1111}(\dot{\varepsilon}_{22} - \dot{\varepsilon}_{22}^p) + C_{1133}\dot{\varepsilon}_{33}, \\
\dot{\sigma}_{33} &= C_{1133}(\dot{\varepsilon}_{11} - \dot{\varepsilon}_{11}^p) + C_{1133}(\dot{\varepsilon}_{22} - \dot{\varepsilon}_{22}^p) + C_{3333}\dot{\varepsilon}_{33}, \\
\dot{\sigma}_{23} &= 2C_{2323}(\dot{\varepsilon}_{23} - \dot{\varepsilon}_{23}^p), \\
\dot{\sigma}_{13} &= 2C_{2323}(\dot{\varepsilon}_{13} - \dot{\varepsilon}_{13}^p), \\
\dot{\sigma}_{12} &= \left(C_{1111} - C_{1122}\right)(\dot{\varepsilon}_{12} - \dot{\varepsilon}_{12}^p).
\end{aligned} \tag{7}$$

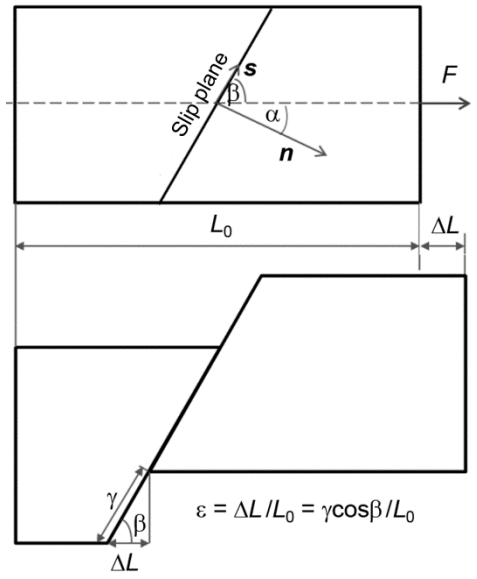

Fig. 2. Geometric interpretation of crystal plasticity relations (Eq. (8)).

Tensor components $\dot{\varepsilon}_{ij}$ of total strain rates are determined by kinematic relations from Eq. (3) depending on the displacement velocities only. The derivation of tensor $\dot{\varepsilon}_{ij}^{p}$ of plastic strain rates from Eq. (4) is associated with physical models constructed with account of plastic deformation mechanisms operating at the selected scales. Within the crystal plasticity, the main mechanism of plastic deformation in single crystals is the dislocation motion in the active slip systems and twinning, in particular case. The plastic strain rate components geometrically relate to plastic shear strains in active slip systems (Fig. 2):

$$\dot{\varepsilon}_{ij}^{p} = \sum_{\alpha} \dot{\gamma}^{(\alpha)} \Theta_{ij}^{(\alpha)} , \tag{8}$$

where $\dot{\gamma}^{(\alpha)}$ is the shear strain rate in α slip system,

$$\Theta_{ij}^{(\alpha)} = \frac{1}{2}\left(s_i^{(\alpha)} n_j^{(\alpha)} + s_j^{(\alpha)} n_i^{(\alpha)} \right) \tag{9}$$

is the orientation tensor for α slip system determining its orientation through the components of slip direction $s_i^{(\alpha)}$ and slip plane normal vectors $n_i^{(\alpha)}$ in the orthogonal coordinate system x_i.

In terms of the numerical simulation, the orientation tensor components are expressible through Miller indices that determine slip systems. Let us write Eq. (9) for an arbitrary slip system α given by $\left(h_1 k_1 l_1\right)$ crystallographic plane and $[h_2 k_2 l_2]$ direction. In HCP crystals, Miller indices for the direction normal to $\left(h_1 k_1 l_1\right)$ crystallographic plane are determined by

$$h_2 = 2h_1 + k_1 ,\ k_2 = h_1 + 2k_1 ,\ l_2 = \left(\frac{a}{c}\right)^2 \frac{3}{2} l_1 . \tag{10}$$

The point coordinates given in the orthogonal and crystallographic coordinate systems x_i and x_i^{Xtal} are connected by the following relations:

$$x_1 = \frac{\sqrt{3}}{2} x_1^{\text{Xtal}},\ x_2 = x_2^{\text{Xtal}} - \frac{x_1^{\text{Xtal}}}{2},\ x_3 = (c/a) x_3^{\text{Xtal}}. \tag{11}$$

Substituting Eq. (10) in Eq. (11), we obtain the equation for $n_i^{(\alpha)}$ normal components:

$$n_1 = \frac{x_1^n}{\sqrt{(x_1^n)^2 + (x_2^n)^2 + (x_3^n)^2}},\ n_2 = \frac{x_2^n}{\sqrt{(x_1^n)^2 + (x_2^n)^2 + (x_3^n)^2}},\ n_3 = \frac{x_3^n}{\sqrt{(x_1^n)^2 + (x_2^n)^2 + (x_3^n)^2}}, \tag{12}$$

where $x_1^n = \frac{\sqrt{3}}{2}\left(2h_1 + k_1\right)$, $x_2^n = \frac{3}{2} k_1$, $x_3^n = \frac{a}{c}\frac{3}{2} l_1$. In the same way we find the coordinates for the slip direction vector $s_i^{(\alpha)}$:

$$s_1 = \frac{x_1^s}{\sqrt{(x_1^s)^2 + (x_2^s)^2 + (x_3^s)^2}},\ s_2 = \frac{x_2^s}{\sqrt{(x_1^s)^2 + (x_2^s)^2 + (x_3^s)^2}},\ s_3 = \frac{x_3^s}{\sqrt{(x_1^s)^2 + (x_2^s)^2 + (x_3^s)^2}}, \tag{13}$$

where $x_1^s = \frac{\sqrt{3}}{2} h_2$, $x_2^s = \frac{\left(2k_2 - h_2\right)}{2}$, $x_3^s = (c/a) l_2$.

Based upon Eqs. (12) and (13), orientation tensor components for $\left(h_1 k_1 l_1\right)[h_2 k_2 l_2]$ arbitrary slip system in the HCP crystal can be expressed by the Miller indices as

$$\Theta_{11}^{(\alpha)} = \frac{1}{Q}\frac{3}{4}\left(2h_1 + k_1\right)h_2,\ \Theta_{22}^{(\alpha)} = \frac{1}{Q}\frac{3}{4} k_1 (2k_2 - h_2),\ \Theta_{33}^{(\alpha)} = \frac{1}{Q}\frac{3}{2} l_1 l_2,$$

$$\Theta_{12}^{(\alpha)} = \frac{\sqrt{3}}{4Q}\left(2h_1 k_2 + k_1 h_2 + k_1 k_2 - h_1 h_2\right), \tag{14}$$

$$\Theta_{13}^{(\alpha)} = \frac{\sqrt{3}}{4Q}\left(\frac{c}{a}\left(2h_1 + k_1\right) l_2 + \frac{3}{2}\frac{a}{c} l_1 h_2\right),$$

$$\Theta_{23}^{(\alpha)} = \frac{3}{4Q}\left(\frac{c}{a} k_1 l_2 + \frac{a}{2c}\left(2k_2 - h_2\right) l_1\right),$$

where $Q = \sqrt{(x_1^n)^2 + (x_2^n)^2 + (x_3^n)^2}\sqrt{(x_1^s)^2 + (x_2^s)^2 + (x_3^s)^2}$.

In many works, the shear strain rate $\dot{\gamma}^{(\alpha)}$ is described by viscoplastic models [1], where $\dot{\gamma}^{(\alpha)}$ is the function of resolved shear stress $\tau^{(\alpha)}$:

$$\dot{\gamma}^{(\alpha)} = \dot{\gamma}_0 \left| \frac{\tau^{(\alpha)}}{\tau_{\text{CRSS}}^{(\alpha)}} \right|^{\text{v}} \text{sign}\left(\tau^{(\alpha)}\right), \tag{15}$$

where $\dot{\gamma}_0$ is the initial shear strain rate, ν is the strain rate sensitivity exponent. The resolved shear stress in the α slip system can be determined as

$$\tau^{(\alpha)} = s_i^{(\alpha)} \sigma_{ij} m_j^{(\alpha)}. \tag{16}$$

In accordance with Schmid's law, the slip system is active, if the resolved shear stress in it achieves the critical value of $\tau_{\text{CRSS}}^{(\alpha)}$. The critical resolved shear stress τ_{CRSS} is the most important parameter of the crystal plasticity. The modern literature on the evolution of critical resolved shear stresses shows a variety of models considering different mechanisms of strain hardening and softening, microstructure and phase composition of the material, interaction between dislocations in different slip systems, dislocation kinetics, scaling factor, loading history, and so on [1]. Apparently, the more complex is the model, the wider is the spectrum of physical phenomena the model is able to describe. Physically-based models certainly contain a great deal of constants and parameters that are difficult to determine and considerably complicate the numerical analysis. From the viewpoint of efficiency of numerical experiments, interesting is the development of phenomenological models describing a certain range of physical phenomena at a given scale. In order to define the resolved critical shear stresses in the active slip systems of titanium, we offer the phenomenological dependence of strain hardening and grain-boundary strengthening mechanisms in the form of additive contributions:

$$\tau_{\text{CRSS}}^{(\alpha)} = \tau_0^{(\alpha)} + k_1 D_i^{-1/2} + k_2 \varepsilon_{\text{eq}}^p. \tag{17}$$

Here $\tau_0^{(\alpha)}$ is the resolved critical shear stress in a single crystal. The second term of the sum is the Hall–Petch relationship, which considers the increase in the yield stress of polycrystals owing to the grain boundaries preventing the dislocation motion. In the numerical simulation, the grain diameter D_i is calculated as a diameter of a sphere of the same volume. The third term of the sum is the function of accumulated equivalent plastic strain, which considers the increase in resolved critical shear stresses due to strain hardening. The coefficients k_1 and k_2 of the grain-boundary strengthening and strain hardening can be obtained from experimental stress-strain curves for polycrystalline titanium with a given grain size.

In commercially pure titanium, potentially active are three prismatic, three basal, six $\langle a \rangle$-pyramidal, twelve $\langle c+a \rangle$-pyramidal and six $\langle c+a \rangle$-pyramidal slip systems, as shown in Fig. 1*b*. It is significant that in titanium, resolved critical shear stresses initiating slip in different slip systems differ by several times and considerably depend on the content of alloying elements, including oxygen [10, 12]. In pure titanium consisting less than 0.2% of oxygen, the primary and secondary slip systems are prismatic and basal, respectively [8, 12]. The former have minimum τ_{CRSS} value. According to [8, 12], $\langle a \rangle$-pyramidal slip systems insignificantly affect the deformation process. Under quasi-static deformation at room temperature, $\langle c+a \rangle$ slip does not occur and thus is not considered in the model as well as a twinning mechanism which provides deformation $\dot{\varepsilon}_{33}^p$ along the prismatic axis in the HCP crystal at elevated temperatures, high strain rates, severe plastic deformation and other specific loading conditions [10].

1.3. Polycrystalline titanium model and numerical simulation

The model of the polycrystalline structure is based on the experimental data of the electron backscatter diffraction (EBSD) analysis of commercially pure titanium presented in [13, 14]. The orientation imaging microscopy (OIM) shows that the structure of non-deformed titanium specimens consists of ~70 μm equiaxed grains (Fig. 3*a*). The analysis of pole figures displaying the crystallographic texture before and after deformation as given in Fig. 3*b*, shows the basal texture with the misorientation angle of about 40 degrees, which is common to rolled titanium.

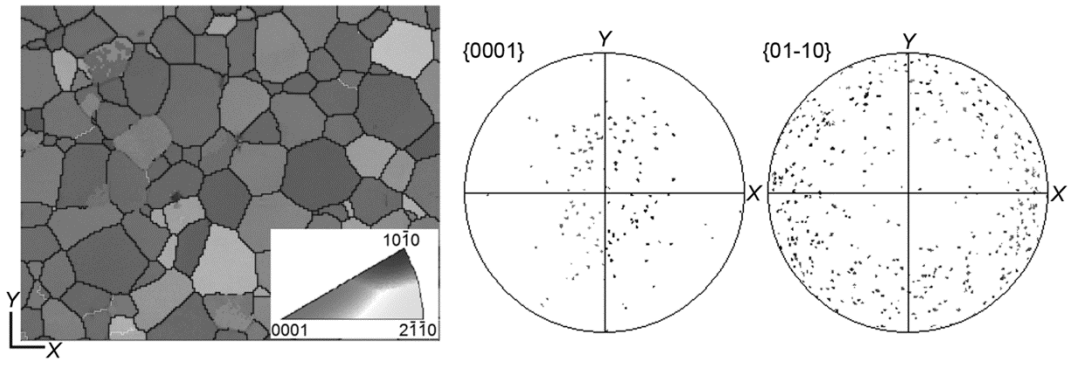

Fig. 3. OIM map (*a*) and pole figures (*b*) of pure titanium microstructure [14].

The polycrystalline structure is generated by the step-by-step packing (SSP) method [15]. The idea is to incrementally fill the computational domain preliminary discretized by a computational mesh with structural elements, in conformity with the analytically specified growth-rate functions, such as equations of sphere, ellipsoid, cylinder, *etc*. The initial conditions include the spatial distribution of nuclei, *i.e.* centers of growing structural elements (grains). In the simplest case of growth in all the elements according to spherical equation at the same rate, the structure generated by the SSP method coincides with the Voronoi diagram representing cells as convex polyhedra [5]. In such models, the grain boundaries are formed by the mesh nodes, while physical-and-mechanical properties of the material are set inside the mesh elements. The groups of contacting elements with the same properties form a grain. The SSP method applied to the generation of various microstructures is described in details in [15].

Based on the experimental data [14], the polycrystalline structure consisting of 3300 quasi-equiaxed grains is generated on a finite element mesh comprising $3.375 \cdot 10^6$ hexahedral elements. The model size is 0.3×0.035×0.1 cm; the average grain size is 70 μm (Fig. 4).

The initial conditions assume that all grains possess similar physical-and-mechanical properties, such as density, elastic moduli, initial resolved critical shear stress, activating dislocation slip, *etc*. and differ only by the orientation of local coordinate systems x_i relative to the global coordinate system X_i associated with the specimen geometry (Fig. 4*a*). Initially, orientation of the local coordinate system is constant within the grain and changes when crossing the grain boundary. Orientations of the local coordinate systems relative to the global coordinate system are given by Euler angles, such that to simulate the basal texture according to the experimental data (cf. Figs 3*b* and 4*b*). Calculations are also made for the non-textured microstructure, for which the grain orientation is determined by a set of Euler angles defined by a random number generator (Fig. 4*c*).

The boundary value problem of uniaxial tension of the modeled polycrystalline structures is solved by the finite element (FE) method using the ABAQUS/Explicit. FE calculations of uniaxial tension are carried out in terms of the dynamic problem using parallel algorithm. A constitutive model based on the crystal plasticity obtained for HCP crystals, is introduced in the ABAQUS/Explicit *via* VUMAT user subroutine, where Eqs. (7)–(17) are solved by an iteration method.

The tension along X_1-axis is given in Eq. (5) (Fig. 4*a*). In order to minimize the dynamic effect, the load is linearly increased up to the peak value, and then kept constant. On the bottom surface, the symmetry conditions are set relative to X_3-axis. The rest surfaces are considered to be unaffected by external forces.

It is important to underline that Eqs. (1)–(3) and boundary conditions in Eqs. (5) and (6) are formulated and solved in the global coordinate system (Fig. 4*a*), whereas the constitutive relations – in the local coordinate system (see Fig. 1*a*). The calculation algorithm includes the following steps:

1) solution of Eqs. (1)–(3), (5), (6) in the global coordinate system;

2) transformation of the total strain rate tensor components to the local coordinate system and solution of constitutive relations in the crystal system of coordinates;

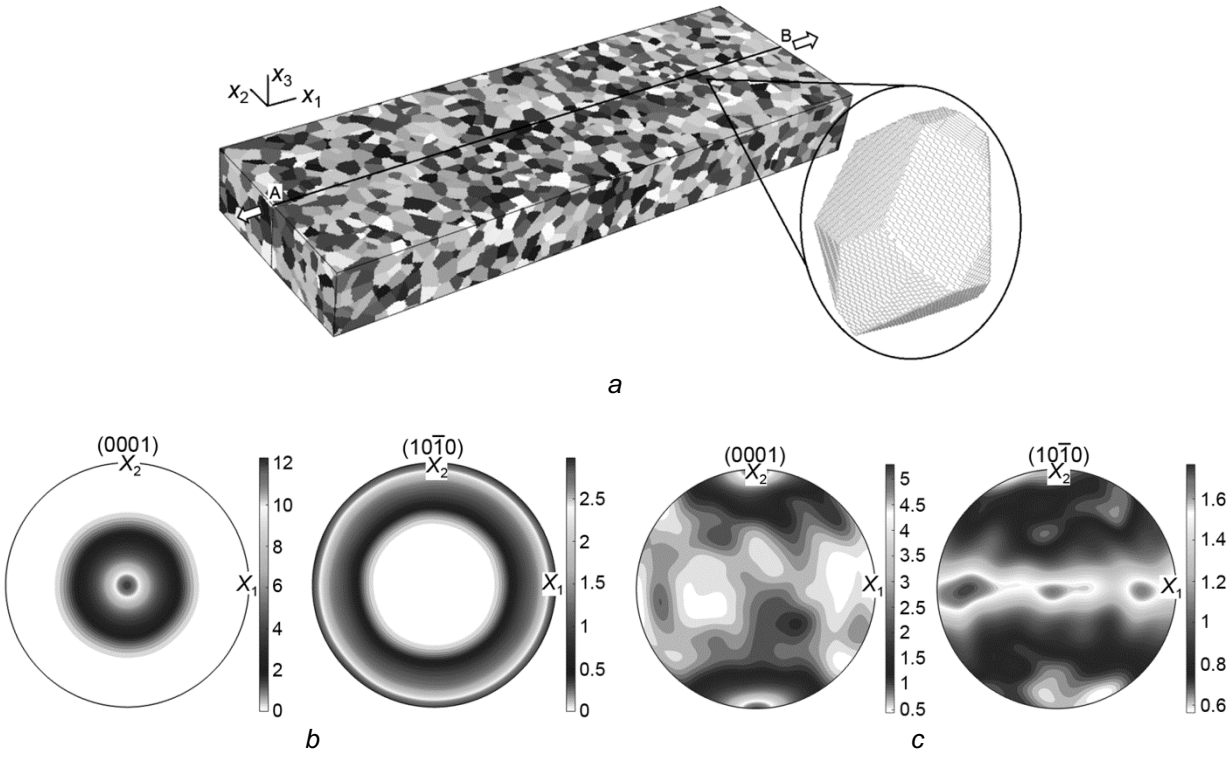

Fig. 4. Polycrystalline titanium model (*a*) and pole figures displaying textured (*b*) and non-textured (*c*) microstructure.

3) inverse transformation of the obtained stress tensor components to the global coordinate system and a transfer to a new time step.

2. SIMULATION RESULTS

2.1. Analysis of single crystal uniaxial tension

The model testing includes the analysis of uniaxial tension of titanium single crystals with three different crystallographic orientations relative to the loading axis as schematically shown in Fig. 5*a–c*. A 5×5×10 mm geometrical model is approximated by a regular FE mesh consisting of 31250 hexahedral elements. The values of elastic moduli and resolved critical shear stresses for different slip systems are summarized in Table 1. Strain hardening is not considered in calculations. In this case, it is possible to compare the stress-strain parameters in crystals having different crystallographic orientation with analytical data and expected geometry of active slip systems. The calculated yield stress values are compared with analytical values obtained from Schmid's law:

$$\sigma_y = \frac{\tau_0}{\cos\lambda\cos\phi}, \tag{18}$$

where τ_0 is the resolved shear stress, σ_y is the equivalent stress, λ is an angle between the loading axis and the normal to the slip plane, ϕ is an angle between the loading axis and the direction of slip.

In all modeled single crystals, plastic deformation occurs due to slip on prismatic slip systems. In Fig. 5*a–c,* one can see one of the prismatic slip systems. Due to the symmetry of the crystal lattice, orientation of other prismatic

TABLE 1. Material Constants and Model Parameters

C_{1111}, GPa	162
C_{1133}, GPa	92
C_{1122}, GPa	69
C_{3333}, GPa	181
C_{2323}, GPa	47
$\tau_0^{\text{prismatic}}$, MPa	50
τ_0^{basal}, MPa	100
$\tau_0^{\text{pyramidal}}$, MPa	180
k_1, MPa ·cm$^{1/2}$	0.664
k_2, MPa	50.0

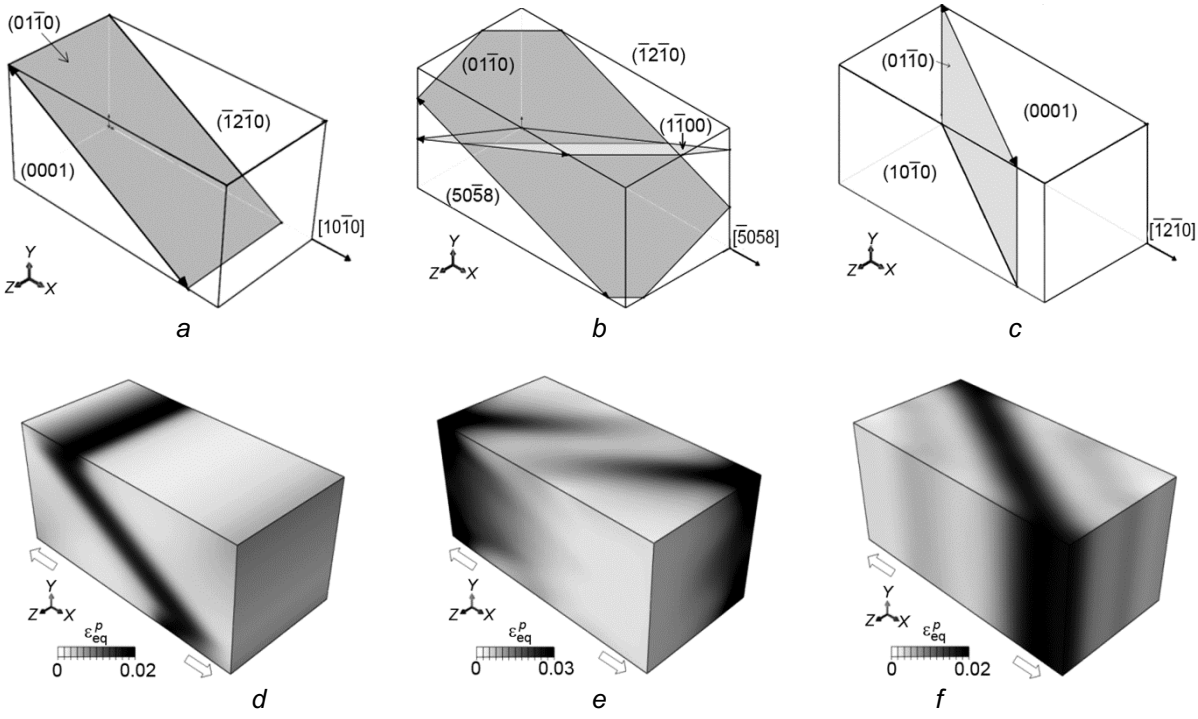

Fig. 5. Three-dimensional simulation of single crystals with different orientations (*a–c*) and respective equivalent plastic strain distributions at 0.5% tensile strain (*e–f*).

slip systems is determined by the incremental rotations to an angle of 60 degrees relatively [0001] axis. The analytical vs. numerical values of the yield stress are given in Table 2 for the modeled crystals with different orientation. The analytical values of σ_y are obtained from Eq. (18), while the numerical values $<\sigma_{eq}>$ are the equivalent stresses averaged over specimens. The difference between the analytical and numerical values is not over 0.2% that confirms correctness of the model and numerical implementation.

Analytically, in each of the studied crystallographic orientations, two of three prismatic slip systems are equally loaded and their activation must occur simultaneously under the same stress applied (see Table 2). In the case of no hardening, at the initial stage of loading, plastic deformation localizes throughout the thickness of macroscale shear band, whose orientation coincides with that of one of the prismatic slip systems for all the studied single crystals.

TABLE 2. Yield Stress in HCP Single Crystals with Different Orientation

Orientation	Analytical value σ_y, MPa	Numerical value $<\sigma_{eq}>$, MPa
Fig. 5*a*	138.56	138.42
Fig. 5*b*	275.42	275.35
Fig. 5*c*	138.56	138.38

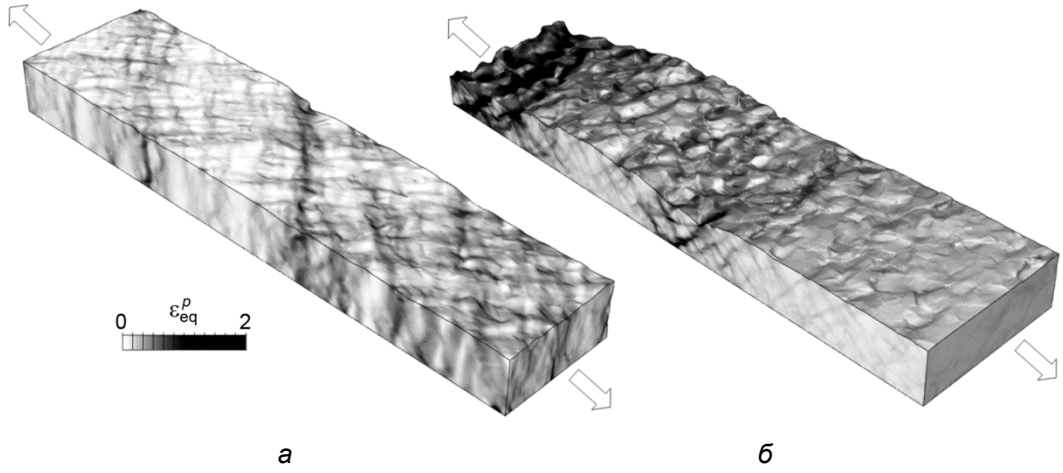

Fig. 6. Equivalent plastic deformations in textured (*a*) and non-textured (*b*) polycrystals at a 20% tensile strain.

Deformation in the macroscale shear band is caused by dislocation glide in all active slip systems, but the most serious contribution belongs to the slip system of the respective orientation.

2.2. Influence of texture on localized plastic deformation in polycrystal models

The FE analysis is provided for both textured and non-textured polycrystals with a glance to strain hardening and grain-boundary strengthening. The data from Table 1 are used in FE calculations. Localized plastic deformations shown in Fig. 6 for textured and non-textured polycrystals demonstrate significant difference.

In the case of the non-textured microstructure, there are two distinct scales of plastic strain localization. At a microscale, we observe in-grain and near-grain boundary plastic strain localization. It should be noted that although this approach does not explicitly consider the dislocation motion, the model describes in-grain plastic strain localization controlled by the lattice orientation, as illustrated in Fig. 5 for single crystals. The surface roughness of non-textured material is provided by the out-of-plane surface displacement of neighbor grains relatively each other. Such a deformation-induced surface roughness is observed in many materials and called orange peel (*e.g.* [16, 17]). Along with the microscale roughness, the surface is characterized by non-crystallographic mesoscale shear bands passing across the surface normal to the axis of tension.

In the case of textured microstructure, mesoscale shear bands appear on the surface already at the initial stage of plastic flow. During tension, the angle between the shear bands and the tensile axis changes from 50 to 45 degrees. The microscale roughness provided by the out-of-plane surface displacement of individual grains and grain clusters, is ill-defined during the whole deformation process.

Let us analyze the detected differences concerning the dislocation glide in the modeled microstructures. HCP crystals are characterized by significant anisotropy of plastic properties. There are two grain orientations affecting the microstructure ability to dislocation glide. When the load is parallel to basal planes, the grain is easily involved in

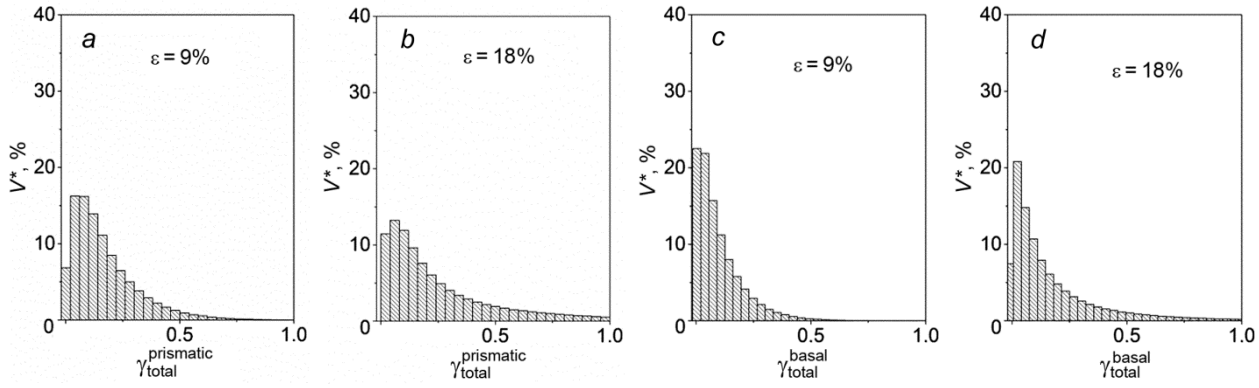

Fig. 7. Bar graphs of slip accumulated on prismatic (*a*, *b*) and basal (*c*, *d*) slip systems of non-textured microstructure.

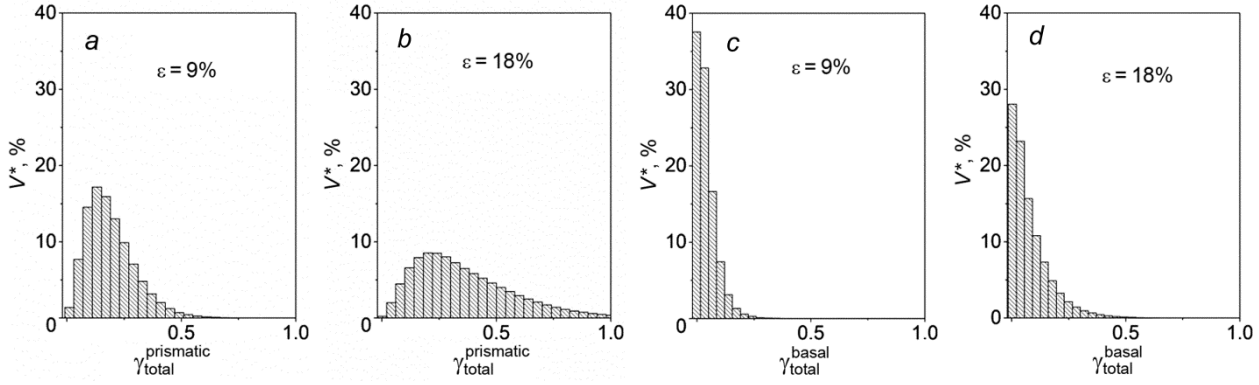

Fig. 8. Bar graphs of slip accumulated on prismatic (*a*, *b*) and basal (*c*, *d*) slip systems of basal texture microstructure.

plastic deformation owing to the dislocation glide on favorably oriented prismatic slip systems. On the contrary, when the load is parallel to the prismatic crystal axis, the grains cannot be deformed by the dislocation glide. The grains of intermediate orientation are more or less involved in the dislocation glide. In [13, 14] it is shown that strain accommodation of unfavorably oriented grains can occur due to both their rigid rotation and plastic deformation of favorably oriented neighbor grains. A non-textured microstructure always contains favorably oriented grains, which can provide the given deformation. And a textured microstructure enables the formation of directions in which deformation is either easy or difficult. In the case of a basal texture, a slip normal to the specimen surface is difficult because this direction matches the preferential orientation of prismatic axes of grains.

Let us discuss the change in prismatic and basal slip contributions to plastic deformation of textured and non-textured polycrystals. This is shown in Figs 7 and 8 containing bar graphs representing the amount of slip in the respective slip systems calculated for each finite element as

$$\gamma_{\text{total}}^{\alpha} = \sum_{\alpha=1}^{3} \int_{t} \left| \dot{\gamma}^{\alpha} \right| dt \,, \tag{19}$$

where summation is made by three prismatic or three basal slip systems. The volume fraction V^* of the material is on *y*-axis and expressed as a percentage.

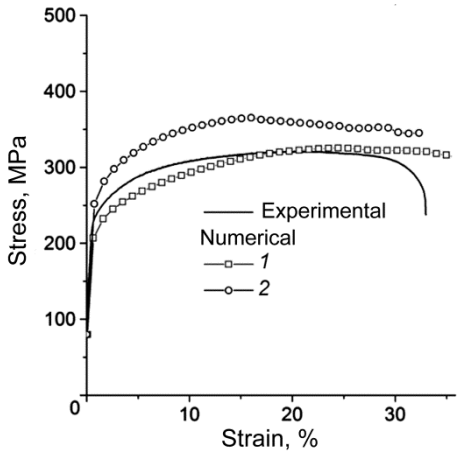

Fig. 9. Calculated vs. experimental [13] stress-strain curves of polycrystal models.

In both models, the dislocation glide on prismatic slip systems activates at an earlier stage of tension and contributes much to deformation throughout the whole process, which is in agreement with the experimental data [7, 8]. But the ratio between prismatic and basal slip substantially depends on the texture. The total slip accumulated on prismatic slip systems in non-textured microstructure of the half-volume polycrystal ranges from 4 to 16% at a 9% deformation degree and from 6 to 22% at a deformation degree of 18%. In the microstructure with a basal texture, the amount of prismatic slip is higher. Thus, at a 9% deformation degree, over 60% of the material manifest prismatic slip varying from 10 to 20%, while in localized regions, the total prismatic slip reaches 50%. When the deformation degree is 18%, the total prismatic slip varies between 10 and 50%, and in 10% of the material it reaches 70% and over.

Basal slip systems become active at a later stage of tension and less contribute to the deformation process. But in the case of the basal texture, at a 9% deformation degree, the slip amount in basal slip systems is negligible, namely it is not over 6% in a half the material, and zero in the rest. When deformation increases up to 18%, the amount of basal slip grows up to 3–10% in 40% of the material, but is still insignificant as compared to the contribution from prismatic slip systems. In the non-textured microstructure the ratio between basal and prismatic slip can be measured already at a 9% deformation degree, when about 50% of the material is subjected to basal slip ranging from 3 to 10%. At a deformation degree up to 18%, only 7% of the material is not subjected to basal slip, while in 50% of grains the accumulated basal slip ranges from 2 to 12%.

Figure 9 presents the stress-strain curves calculated for both textured and non-textured microstructures compared with the experimental data [14]. The numerical curve for the basal microstructure is in agreement with the experimental data on pure titanium with the similar texture (see Fig. 3) that proves a correct choice of the model parameters. The numerical curve for the non-textured microstructure is higher, which is also in agreement with the experimental data [8]. Despite the fact that strain hardening of grains is set to be low (see Table 1) in the linear function models (Eq. (17)), the stress-strain curves have a parabolical section next to the elastic stage. This is due to a gradual involvement of differently-oriented grains relatively the load axis in plastic deformation.

CONCLUSIONS

In terms of micromechanics and crystal plasticity, the deformation behavior of polycrystalline titanium was numerically investigated. The polycrystalline model generated by the method of step-by-step packing was introduced in FE calculations in an explicit form. The model describing the plastic behavior of grains was proposed on the basis of the crystal plasticity, which considered anisotropy of elastoplastic properties at the microscale. Anisotropy of properties was provided by the specific crystallographic structure and dislocation glide in the material. The proposed model was used to study the texture influence on localized plastic deformation in polycrystals.

It was found that the presence of basal texture prevented microscale roughening caused by out-of-plane displacements of individual grains and grain clusters. At the mesoscale, localized shear bands of non-crystallographic nature formed on the textured surface at an angle of 45–50 degrees to the axis of tension already at the beginning of plastic deformation.

In the polycrystal with the non-textured structure, the well-defined deformation-induced roughness developed at the microscale due to shear of individual grains and their clusters normal to the free surface. Along with the microscale roughness, mesoscale-localized plastic deformation developed in the form of non-crystallographic shear bands crossing the whole specimen surface normal to the axis of tension.

This work was performed within the frame of the Fundamental Research Program of the State Academies of Sciences for 2013–2020, research line III.23.

REFERENCES

1. F. Roters, *et al*., Acta Mater., **58**, 1152–1211 (2010).
2. P. S. Volegov, D. S. Gribov, and P. V. Trusov, Phys. Mesomech., **20,** 174–184 (2017).
3. P. V. Trusov and N. S. Kondratyev, Phys. Mesomech., **22**, 230–241 (2019).
4. H. Zhang, J. Liu, D. Sui, *et al*., Int. J. Plasticity, **100,** 69–89 (2018).
5. N. Vajragupta, *et al*., Phys. Mesomech., **20**, 343–352 (2017).
6. M. Diehl, *et al*., Phys. Mesomech., **20,** 311–323 (2017).
7. F. Bridier, P. Villechaise, and J. Mendez, Acta. Mater., **53**, No. 3, 555–567 (2005).
8. J. W. Won, K.-T. Park, S.-G. Hong, and C. S. Lee, Mat. Sci. Eng. A-Struct., **637,** 215– 221 (2015).
9. Yu. P. Sharkeev, A. Yu. Eroshenko, Zh. G. Kovalevskaya, *et al*., Russ. Phys. J., **59,** No. 3, 930–934 (2016).
10. S. Zaefferer, Mat. Sci. Eng. A-Struct., **344,** No. 1–2, 20–30 (2003).
11. V. A. Romanova, *et al*., Phys. Mesomech., **22,** 296–306 (2019).
12. J. Q. Ren, *et al*., Mat. Sci. Eng. A-Struct., **731**, 530–538 (2018).
13. A. V. Panin, *et al*., Phys. Mesomech., **21**, 249–257(2018).
14. V. Romanova, *et al*., Mat. Sci. Eng. A-Struct., **697**, 248–258 (2017).
15. V. Romanova and R. Balokhonov, Eng. Comput., (2019). DOI: 10.1007/s00366-019-00820-2.
16. M. L. Miranda-Medina, Surf. Eng., **31**, 519–525 (2015).
17. K. Yoshida, Int. J. Mech. Sci., **83**, 48–56 (2014).